# Fault Classification of Power Distribution Cables by Detecting Decaying DC Components With Magnetic Sensing

Ke Zhu and Philip W. T. Pong

***Abstract*— Fault classification of power distribution cables is essential for tripping relays, pinpointing fault location, and repairing failures of a distribution network in the power system. However, existing fault-classification techniques are not totally satisfactory because they may: 1) require the precalibration of responding threshold for each network; 2) fail to identify the three-phase short-circuit faults. since some electrical parameters (e.g., phase angle) are still symmetrical even in abnormal status; and 3) be invulnerable of electromagnetic interferences. In this paper, a fault-classification technique by detecting decaying dc components of currents in faulted phases through magnetic sensing is proposed to overcome the shortcomings mentioned above. First, the three-phase currents are reconstructed by magnetic sensing with a stochastic optimization algorithm, which avoids the waveform distortion in the measurement by current transformers that incurred by the dc bias. Then, the dc component is extracted by mathematical morphology (MM) in phase currents to identify the fault type together with the polarity of dc components. This method was verified successfully for various fault types on a 22-kV power distribution cable in simulation and also a scaled power distribution network experimentally. The proposed method can enhance the reliability of the power distribution network and contribute to smart grid development.**

***Index Terms*— DC component, fault classification, magnetic sensing, power distribution cable, smart grid.**

## I. Introduction

A RELIABLE power distribution system is crucial for ensuring the reliability and stability of electricity delivery to customers [1], [2]. Power distribution cables are typically deployed underground instead of being overhead because this layout makes them less susceptible to outages under harsh weather conditions (e.g., high wind thunderstorms, heavy snow, and ice storms) and for the sake of aesthetic purpose [3]. However, short-circuit faults still occur on power distribution networks due to internal insulation breakdown or external damage. For example, a screening fault is an insulation breakdown that results in the physical contact between phase conductors and the screen [4]. As the screen is grounded, a phase-to-ground fault occurs. The insulation between conductors can breakdown due to corrosion, leading to a phase-to-phase short-circuit fault. It would be a phase-phase-to-ground short-circuit fault if the screening is also involved. An accidental excavation on the underground power cable can lead to a three-phase short-circuit fault and an explosion as well [5]. The consequence of short-circuit faults can be very serious. First, the excessive heating of the cables can result in fire and explosion. Moreover, a cascade tripping or shutdown can happen in a power system. As such, the short-circuit fault should be cleared up by relays within the shortest time to reduce the adverse effects.

To trip relays properly, a very critical step after detecting the short-circuit fault is to classify its type [6], [7]. This is because the corresponding protection scheme should be executed immediately to clear the fault, minimize the effects, and recover the system. For example, a single-phase reclosing is executed to trip and reclose the faulted phase for extinguishing the arcs and recovering the systems, rather than to trip irrelevant phases. The short-circuit fault type can also be used to infer the cause of faults. Therefore, an accurate and reliable fault classification for clearing and analyzing the faults in the power system is significant.

Though a series of fault-classification techniques has been proposed so far, these methods [8]–[12] suffer some problems as summarized in Table I. First, most of the techniques require precalibration for responding threshold, which accounts for 30% of the total capital cost of the workforce on setting relay thresholds [13], [14]. For example, the threshold is set as a larger number (e.g., 1.5 times) as the steady current in the overcurrent method [15], [16]. This cost is becoming increasingly daunting when the electricity consumption and power distribution network are drastically expanding over the world [17]. Moreover, some of these techniques may be vulnerable to electromagnetic interference (EMI) from the background. This may lead to the erroneous fault classification that is attributable to the electromagnetic coupling between the faulted and healthy phases [18]. This problem can become even more severe with a larger number of high-frequency electronic devices used nearby nowadays. Besides, the

Manuscript received January 18, 2019; revised May 18, 2019; accepted May 30, 2019. Date of publication June 12, 2019; date of current version April 7, 2020. This work was supported by the Seed Funding Program for Basic Research, Seed Funding Program for Applied Research and Small Project Funding Program from the University of Hong Kong, ITF Tier 3 funding under Grant ITS/203/14, Grant ITS/104/13, and Grant ITS/214/14, in part by RGC-GRF under Grant HKU 17210014 and Grant HKU 17204617, and in part by the University Grants Committee of Hong Kong under Contract AoE/P-04/08. The Associate Editor coordinating the review process was Guglielmo Frigo. *(Corresponding author: Philip W. T. Pong.)*

The authors are with the Department of Electrical and Electronic Engineering, The University of Hong Kong, Hong Kong (e-mail: zhuke@hku.hk; ppong@eee.hku.hk).

Color versions of one or more of the figures in this article are available online at http://ieeexplore.ieee.org.

Digital Object Identifier 10.1109/TIM.2019.2922514

TABLE I
ANALYSIS OF EXISTING FAULT-CLASSIFICATION METHODS

| Method | Principle | No need of pre-calibration | Applicable for three-phase short circuit | Invulnerable of EMI | Reasons |
|---|---|---|---|---|---|
| **Overcurrent method [15]** | Large current arises in faulted phase | ×* | √ | √ | * The threshold setting for discriminating overcurrent depends on each network. |
| **Angular difference method [8]** | Different fault results in different characteristics of $\Delta\omega_{AB}$, $\Delta\omega_{BC}$, and $\Delta\omega_{AC}$ | √ | ×* | √ | * Angular difference between phases ($\Delta\omega_{AB}$, $\Delta\omega_{BC}$, and $\Delta\omega_{AC}$) is still symmetrical in three-phase short-circuit fault. |
| **Phase difference method [12]** | Different fault results in various characteristics of $\Delta I_{AB}$, $\Delta I_{BC}$, and $\Delta I_{AC}$ ($\Delta V_{AB}$, $\Delta V_{BC}$, and $\Delta V_{AC}$) | √ | ×* | √ | * Current (voltage) difference between phases ($\Delta I_{AB}$, $\Delta I_{BC}$, and $\Delta I_{AC}$ or $\Delta V_{AB}$, $\Delta V_{BC}$, and $\Delta V_{AC}$) is still symmetrical in three-phase short-circuit fault. |
| **Current-wavelet-spectrum method [9]** | Faulted current carries a specific wavelet spectrum which is different from healthy phase | ×*(1) | √ | ×*(2) | *(1) Wavelet spectrum depends on system configuration.<br>*(2) EMI in power system can affect wavelet spectrum pattern. |
| **High-frequency energy (10-20 kHz) method [10]** | Frequency spectrum (10-20 kHz) is different between faulted and healthy phase | ×*(1) | √ | ×*(2) | *(1) Spectrum pattern (10-20 kHz) depends on system configuration.<br>*(2) EMI in power system can introduce high-frequency signals in healthy phases. |
| **High-frequency noise (60 kHz) [11]** | A bandwidth around 20 kHz centered on a 60 kHz in faulted phase | √ | √ | ×* | * EMI in power system can introduce high-frequency signals in healthy phases. |

accuracy of fault classification needs improvement for identifying the three-phase short-circuit fault. Some techniques in Table I fail to identify such fault, because some electrical parameters (e.g., phase angle) in three-phase short-circuit fault remain symmetrical even in abnormal status. Therefore, a new fault-classification technique is necessary to overcome these problems [19], [20].

In this paper, a fault-classification technique by detecting decaying dc components in fault currents with magnetic sensing is proposed, which overcomes the problems mentioned above. In Section II, the analysis of dc component in power distribution networks and the process of extracting dc components from phase currents based on the magnetic sensing are presented. The method is verified by simulation in Section III, and also by experiment in Section IV. The conclusion and future work are drawn in Section V.

## II. METHODOLOGY

The dc component arises in the faulty phase when the short-circuit fault occurs. The analysis of dc components for the power distribution network and the process of extracting the dc components of phase current from magnetic sensing are present as follows.

### A. DC Component in Fault Currents

There is a sudden current change in the faulted phase when a short-circuit fault occurs on the distribution line. A decaying dc component arises because the current cannot change instantaneously since the power network is highly inductive for its composition of many generators and transformers [21], [22]. For calculating the dc component after short-circuit fault, an equivalent circuit of a power distribution network (Fig. 1) under a phase-to-ground short-circuit fault (A-G) is analyzed as follows. The short-circuit point is somewhere on the power distribution cable of Phase A connected with a short-circuit

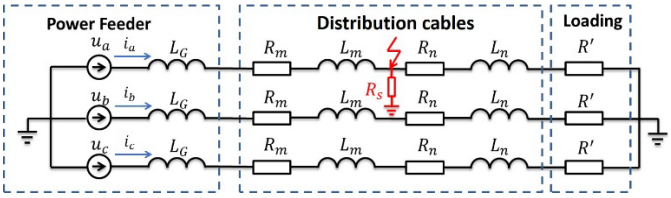


Fig. 1. Equivalent circuit of a power distribution network comprised of power feeder (e.g., generator or transformer), a distribution cable and the loading under a phase-to-ground fault (A-G).

resistor ($R_s$). In the steady status of the network, the current of Phase A ($i_a$) is calculated as [23]

$$i_{a(0)} = I_{m(0)} \sin(\omega t + \alpha - \varphi_0) \tag{1}$$

$$i_{m(0)} = \frac{u_a}{\sqrt{(R_m + R_n + R')^2 + \omega^2 (L_G + L_m + L_n)2}} \tag{2}$$

$$\varphi_0 = \arctan \frac{\omega(L_G + L_m + L_n)}{R_m + R_n + R'} \tag{3}$$

where $u_a$ is the voltage of Phase A, $\alpha$ is the incipient angle of Phase A, and the resistance ($R_m$, $R_n$, and $R'$) and inductance ($L_G$, $L_m$, and $L_n$) of the network can be found in Fig. 1. After the short-circuit fault occurs in Phase A, the differential equation in transient status for Phase A is expressed as

$$(L_G + L_m)\frac{di_a}{d_t} + (R_m + R_p) i_a = u_a \sin(\omega t + \alpha) \tag{4}$$

$$R_p = R_s // \sqrt{(R_n + R')^2 + \omega^2 (L_n)^2} \tag{5}$$

where $R_s$ is the short-circuit resistance. By solving (1)–(5), the short-circuit current of Phase A ($I_a$) is calculated as

$$I_a = I_{sc} + I_{dc} \tag{6}$$

$$I_{sc} = \frac{U_m}{Z} \sin(\omega t + \alpha - \varphi) = I_m \sin(\omega t + \alpha - \varphi) \tag{7}$$

$$Z = \sqrt{(R_m + R_p)^2 + \omega^2 (L_G + L_m)^2} \tag{8}$$

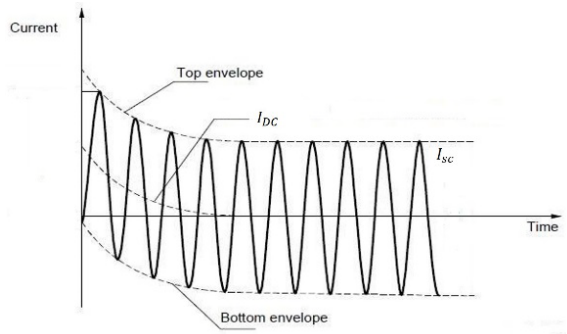


Fig. 2. Decaying dc component in the current of faulted phase over time.

$$\varphi = \arctan \frac{\omega(L_G + L_m)}{R_m + R_p} \tag{9}$$

$$I_{\mathrm{dc}} = (I_{m(0)} \sin(\alpha - \varphi_0) - I_m \sin(\alpha - \varphi)]e^{-t/T_a} \tag{10}$$

$$T_a = \frac{L_G + L_m}{R_m + R_p} \tag{11}$$

where $I_{\mathrm{sc}}$ is the symmetrical component and $I_{\mathrm{dc}}$ is the decaying component in exponential trend in the short-circuit current. Then, the waveform of this short-circuit current is shown in Fig. 2, where this dc component appears in several cycles (depending on the time constant $T_a$) after the fault occurs. This paper focuses on permanent faults that cause the sustained disruption, and thus, this decaying dc component is detectable over the whole duration. As such, the emergence of this dc component can be used for indicating the faulted phase after a fault occurs.

Making use of the dc component in the faulty phase for fault classification can solve the problems shown in Table I. First, no precalibration is required to initialize relays, because this method does not need to determine a responding threshold for different distribution power networks. Second, the dc component only arises under the fault condition but not the normal condition. Third, the dc component is robust, because the EMI in the power system is of high frequency (greater than kilohertz) and does not interfere with the dc component. Therefore, the proposed method of adopting the dc component for fault classification is more reliable.

It is worthwhile to mention that various control strategies are deployed in a power system that may affect the characteristics of fault signals after fault happens. However, the clearing time is typically about 80 ms in which the first 40 ms (two cycles) refers to the fault detection, classification, and trip decision, and the last 40 ms to initiate the system control [24]. Therefore, the proposed technique should work irrespective of different control strategies as the fault signals (i.e., dc decaying components) arise immediately after a fault occurs (the sampling frequency must be high enough such as megahertz to capture the fault signals).

A complete protection process of power system includes fault detection, classification, decision-making, and tripping relay [25], [26]. It is also worth mentioning that our method only works after the successful detection of short-circuit fault. Some fault detection methods of short-circuit fault can be found in [27] and [28]. Our method is intended for fault classification but not fault detection. DC components may occur in some normal operation conditions. For example, dc offset on motor starting can be significant causing tripping of instantaneous breakers [29]. However, this kind of disturbance is not a fault, and there is no need for fault classification.

TABLE II
FACTORS AFFECTING THE PATTERN OF DC COMPONENT

| Parameter | DC component | |
|---|---|---|
| | Initial value | Time constant |
| Incipient angle | * | × |
| Fault resistance | − | − |
| Distance | − | + |
| Feeder voltage | + | × |

### B. Characteristics of DC Component

The pattern of dc component after fault depends on the initial value and decaying time of dc components, as shown in Fig. 2. By further analyzing (1)–(11), it can be found that the characteristics of dc components are correlated with incipient angle [$\alpha$ in (1)], fault resistance [$R_s$ in (5)], fault distance, and the voltage of the feeder. The relations between the initial value (time constant) and these parameters are summarized in Table II (∗: correlated but not linearly; +: positively correlated; −: negatively correlated; and ×: not correlated). Some practical examples are also shown in Fig. 3. From these results, we can conclude that: 1) the initial value of the dc component can change with different fault times but the decaying time remains unchanged; 2) the initial value and decaying time of dc component reduce with a larger fault resistance; 3) the initial value of the dc component decreases when the fault occurs farther away from the front of the cable; and 4) the initial value of the dc component is dominant in a distribution network of higher voltage. The fault time and location are uncontrollable. However, we can see that the proposed method is more efficient in a higher voltage power distribution network under lower resistance fault, as it provides stronger fault signals (i.e., larger initial value and longer lasting time) to be measured.

Based on the results in Fig. 3, it can be seen that the dc component of current does not change too much over fault locations (this is because the unit resistance of the cable is very small). However, the dc component of current indeed changes differently with fault resistance. Some methods in Table I may not work under the condition. For example, the overcurrent method typically sets the threshold of 1.5 times as the standard current [15]. This threshold cannot be reached when the fault resistance is high [e.g., the peak value is only about 1.1 times for a high fault-resistance of 500 Ω in Fig. 3(c)]. However, the proposed method can still detect the fault signals in this high-resistance fault (e.g., the initial value of 10 A and the lasting time is around half a cycle for a high fault resistance

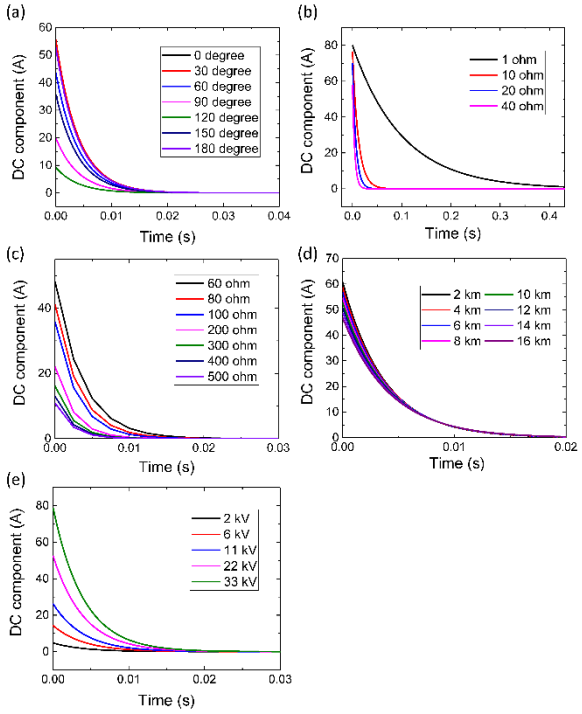


Fig. 3. Study on dc-component characteristics. (a) Effect of incipient angles (line voltage is 22 kV, feeder inductance is 0.0185 Ω, fault resistance is 50 Ω at 10 km of a 20-km cable, unit resistance of the cable is 0.0042 Ω/km, and unit inductance of cable is 0.0016 H/km). (b) Effect of fault resistance at 1, 10, 20, and 40 Ω (line voltage is 22 kV, feeder inductance is 0.0185 Ω, incipient angle is zero, fault occurs at 10 km of a 20-km cable, unit resistance of cable is 0.0042 Ω/km, and unit inductance of cable is 0.0016 H/km). (c) Effect of fault resistance at 60, 80, 100, 200, 300, 400, and 500 Ω (line voltage is 22 kV, feeder inductance is 0.0185 Ω, incipient angle is zero, fault occurs at 10 km of a 20-km cable, unit resistance of cable is 0.0042 Ω/km, and unit inductance of cable is 0.0016 H/km). (d) Effect of fault locations (line voltage is 22 kV, feeder inductance is 0.0185 Ω, the incipient angle is zero, the fault occurs at 50 Ω in a 20-km cable, unit resistance of the cable is 0.0042 Ω/km, and unit inductance of cable is 0.0016 H/km). (e) Effect of feeder voltages (feeder inductance is 0.0185 Ω, the incipient angle is zero, fault resistance is 50 Ω at 10 km of a 20-km cable, unit resistance of the cable is 0.0042 Ω/km, and unit inductance of cable is 0.0016 H/km).

of 500 Ω). The same threshold issue goes for the fault over different times for the overcurrent method [e.g., the peak value is only about 1.1 times when the incipient angle is 120° in Fig. 3(a)]. As such, the proposed method has demonstrated its advantages regarding fault resistance and time.

### C. Fault Classification by DC Component

There are four short-circuit fault types for the power distribution networks, namely, phase-to-ground short-circuit fault, phase-to-phase short-circuit fault, phase-phase-to-ground short-circuit fault, and three-phase short-circuit fault. From the above analysis, the fault type can be identified from the dc component arose in the faulty phase. For example, the fault type (A-G) is identified when there is a dc component found in Phase A but not Phase B or C. However, the dc component exists in two phases both for the phase-to-ground and phase-phase-to-ground faults. As such, the currents of the phase-to-phase and the phase-phase-to-ground faults deserve to be analyzed further as follows.

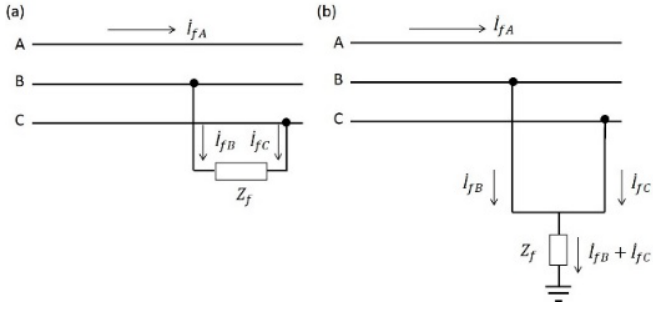


Fig. 4. Short circuit of a three-phase power system. (a) Equivalent circuit of a phase-to-phase short-circuit fault (B-C). (b) Equivalent circuit of a phase-phase-to-ground short-circuit fault (B-C-G).

The equivalent circuits of the phase-to-phase (B-C) and phase-phase-to-ground short-circuit faults (B-C-G) are shown in Fig. 4, respectively. For the phase-to-phase short-circuit fault (B-C), the short-circuit currents are calculated as

$$\dot{I}_{fB} = -\dot{I}_{fC} = \frac{-j\sqrt{3}\dot{U}_{f(0)}}{Z_{\sum 1} + Z_{\sum 2} + Z_f} \tag{12}$$

where $\dot{I}_{fB}$ and $\dot{I}_{fC}$ are the short-circuit currents of Phases B and C, respectively, $\dot{U}_{f(0)}$ is the positive sequence component of voltage at the fault point before the fault occurs, $Z_{\sum 1}$ is the positive sequence impedance in network, $Z_{\sum 2}$ is the negative sequence impedance of network, and $Z_f$ is the short-circuit impedance between Phases B and C. Similarly, the short-circuit currents of phase-phase-to-ground short-circuit fault are calculated as [30], 31]

$$\dot{I}_{fB} = \dot{I}_{f1}\left(a^2 - \frac{Z_{\sum 2} + a(Z_{\sum 0} + 3Z_f)}{Z_{\sum 2} + Z_{\sum 0} + 3Z_f}\right) \tag{13}$$

$$\dot{I}_{fC} = \dot{I}_{f1}\left(a - \frac{Z_{\sum 2} + a^2(Z_{\sum 0} + 3Z_f)}{Z_{\sum 2} + Z_{\sum 0} + 3Z_f}\right) \tag{14}$$

$$\dot{I}_{f1} = \frac{\dot{U}_{f(0)}}{Z_{\sum 1} + \frac{Z_{\sum 2}(Z_{\sum 0}+3Z_f)}{Z_{\sum 2}+Z_{\sum 0}+3Z_f}} \tag{15}$$

$$1 + a + a^2 = 1 \tag{16}$$

where $\dot{I}_{fB}$ and $\dot{I}_{fC}$ are the short-circuit currents of Phase B, and C, $Z_f$ is the short-circuit impedance among Phases B and C and ground, and $Z_{\sum 0}$, $Z_{\sum 1}$, and $Z_{\sum 2}$ are the zero, positive, and negative impedances of the network. Comparing (12)–(16), it can be found that the short-circuit currents of the phase-to-phase fault have the opposite polarity, whereas they are identical for phase-phase-to-ground short-circuit fault. The polarity of dc components would also follow this rule, because they are extracted from the short-circuit currents. As such, the phase-to-phase and phase-phase-to-ground short-circuit fault can be discriminated from the polarity of the dc components.

Therefore, the short-circuit fault type can be identified from the existence and the polarity of dc components in the faulty phases (Table III). When the dc component only exists in one (three) phase, it is identified as a phase-to-ground (three-phase) short-circuit fault. By further looking into the polarity of the

TABLE III
FAULT CLASSIFICATION BASED ON DC COMPONENTS IN SHORT-CIRCUIT CURRENTS

| Fault type | | DC component | | | Polarity |
|---|---|---|---|---|---|
| | | Phase A | Phase B | Phase C | |
| Single-phase-to-ground fault | AG | √ | × | × | Arbitrary |
| | BG | × | √ | × | |
| | CG | × | × | √ | |
| Phase-to-phase fault | AB | √ | √ | × | Opposite |
| | AC | √ | × | √ | |
| | BC | × | √ | √ | |
| Phase-phase-to-ground fault | ABG | √ | √ | × | Identical |
| | ACG | √ | × | √ | |
| | BCG | × | √ | √ | |
| Three-phase fault | ABC | √ | √ | √ | Arbitrary |

dc components, the phase-to-phase and phase-phase-to-ground short-circuit fault can be discriminated.

### *D. Current Reconstruction From Magnetic Sensing*

The commonly deployed current transformers (CTs) cannot measure the dc component in the current, because the dc bias in the magnetizing current can inversely distort the secondary output of the CTs. Though the fiber-optic current sensors (FOCS) are capable of dc measurement, they are typically for high-voltage dc systems (i.e., hundreds of kilovolt) and also very expensive. As such, a computational algorithm for reconstructing the three-phase currents from the magnetic sensing was shown in Fig. 5 [32], [33]. The functional structure diagram of the algorithm is shown in Fig. 5(a), which involves the current and conductor position optimization. The stopping criterion is to evaluate the Euclidean norm between the measured and calculated magnetic fields, which gives [34]

$$\begin{aligned} f(I_p) &= \|AI_p - B_{\text{mea}}\|^2 \\ &= (AI_p - B_{\text{mea}})^T (AI_p - B_{\text{mea}}) \\ &= I_p^T A^T A I_p - 2B_{\text{mea}}^T A I_p + B_{\text{mea}}^T B_{\text{mea}} \end{aligned} \tag{17}$$

where $A$ is the coefficient matrix depending on the optimized conductor position, $I_p$ is the current to be optimized, and $B_{\text{mea}}$ is the measured magnetic fields. The factor $AI_p$ in (17) is equivalent to the optimized magnetic fields based on the Biot–Savart law, which gives

$$B(r) = \frac{\mu_r}{4\pi} \int \frac{dl \times r'}{|r'|^3} I = AI_p \tag{18}$$

where $\mu_r$ is the relative permeability of the medium, $dl$ is the vector along the phase conductor, and $r'$ is the displacement vector of the sensing point from the phase conductor. The minimum is given by the normal equation

$$\nabla f(I_p) = A^T A I_p - A^T B_{\text{mea}} = 0. \tag{19}$$

The solution is then given by

$$I_p = (A^T A)^{-1} A^T B_{\text{mea}}. \tag{20}$$

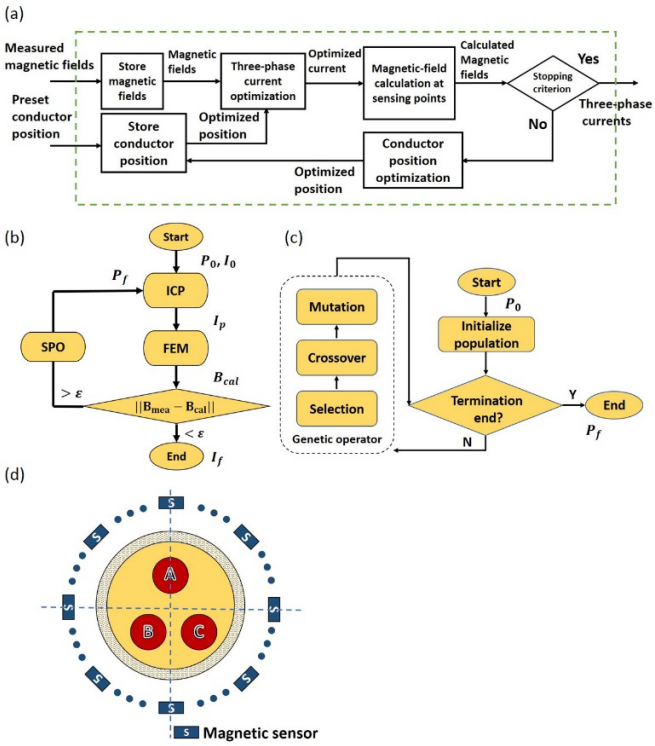


Fig. 5. Three-phase current reconstruction. (a) Functional structure diagram of the algorithm in which three-phase currents are reconstructed via optimization. (b) Flow chart of the whole algorithm. (c) Flowchart of SPO by genetic algorithm. (d) Magnetic-field sensors installed around the three-core power distribution cable.

As such, the current can be optimized by (20). The conductor position is optimized by the genetic algorithm [34]. These steps are repeated until a reasonable error or a maximum number of iterations are reached. Then, the final three-phase currents are finalized. The detailed flowchart of this algorithm is shown in Fig. 5(b), which starts with preassumed positions of the conductors ($P_0$) and currents ($I_0$). The phase currents ($I_p$) are optimized by the inverse current program (ICP) based on (19). The magnetic fields under the optimized currents with the presetting positions can be calculated by the finite-element method (FEM). The final currents ($I_f$) are attained only when the Euclidean distance between the measured ($B_{\text{mea}}$) and calculated ($B_{\text{cal}}$) magnetic fields is smaller than a threshold ($\varepsilon$). This threshold is manually set to represent the allowable error between the calculated magnetic fields under optimized current and position and measured ones. If the threshold is not achieved, the positions of conductors are to be optimized by the source position optimization (SPO). The SPO is embedded with the genetic algorithm, and its details are shown in Fig. 5(c). The genetic algorithm is a search heuristic that reflects the process of natural selection (i.e., selection, crossover, and mutation) [35], [36]. The algorithm begins with a set of conductor position as an initial population. The fittest population reflecting the conductor position under optimized current is selected and crossovered to update. Some of the population is mutated with a low random probability in the case of premature convergence. The algorithm terminates when the population converges. Then, the

fittest phase conductor is chosen for ICP to repeat the process until the threshold ($\varepsilon$) is satisfied. Finally, the three-phase currents are reconstructed from the magnetic fields.

The positions of phase conductors and phase currents need to be tuned in our program. The initial values are critical for achieving the best solutions in the iteration process [35]. Regarding the initial position of three-phase conductors ($P_0$), their phase differences are recommended to be set with 120° differences, and be located in the middle between the cable center and the boundary. The initial currents ($I_0$) are set around the rated value of the cable. The crossover rate is set large (e.g., >0.9) and the mutation rate must be low (e.g., <0.05) in SPO [35]. Moreover, the accuracy of the reconstructed result relies on the magnetic-field measurement [34]. The accuracy can be improved by increasing the number of sensing points [34]. In reality, the magnetic sensors are installed circularly around the cable surface [Fig. 5(d)]. Since magnetic sensors (e.g., low-cost magnetoresistive sensors) can operate from dc to over 1 MHz, the dc components of the three-phase currents can be preserved by this current reconstruction method.

It is worthwhile to mention that the stochastic optimization algorithm only needs to operate when the phase currents and conductor positions are unknown. After determining the positions of phase conductors, the phase currents can be directly solved from the magnetic fields without running the stochastic program again. This step will not induce any artificial dc components in the restored currents unless the magnetic sensors measure asymmetrical magnetic fields due to the actual dc currents.

### *E. DC Component Extraction*

The mathematical morphology (MM) [37], [38] is used to extract the dc component from the reconstructed current. The traditional Fourier transform or the wavelet transform is not used, because they would result in distortion at the front and back ends of the waveform (i.e., the fringe effects) [39]. The basic operations of MM are erosion ($\Theta$) and dilation ($\oplus$), which are defined as

$$(I\Theta B)(x) = \min_{(x+v)\in I, v\in B}[I(x+v) - B(v)] \quad (21)$$

$$(I \oplus B)(x) = \min_{(x-v)\in I, v\in B}[I(x-v) - B(v)] \quad (22)$$

where $I$ is the input current signal, $B$ is the structuring element (the length is a quarter of the fundamental waveform), $x$ corresponds to a pixel in the signal, and $v$ is a pixel in the structuring element [37]. Based on these two operators, the opening ($\circ$) is performed during the peak half cycle, and the closing ($\bullet$) is performed during the trough half cycle as

$$D = \begin{cases} I \circ B & \text{if peak half cycle} \\ I \bullet B & \text{if trough half cycle} \end{cases} \quad (23)$$

where $\circ$ is the opening operator and $\bullet$ is the closing operator. The result of dc extraction for a test function ($y_1 = 5\sin(2*\pi*50*t)$, $y_2 = 10\sin(2*\pi*50*(t-0.3))+20e^{-100(t-0.3)}$) is shown in Fig. 6, and the reconstructed dc component matches with the real dc value.

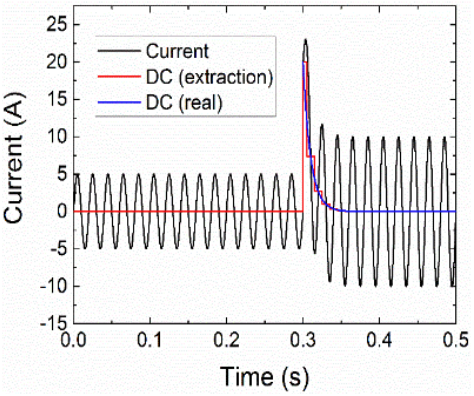


Fig. 6. DC component extraction by mathematical morphology method.

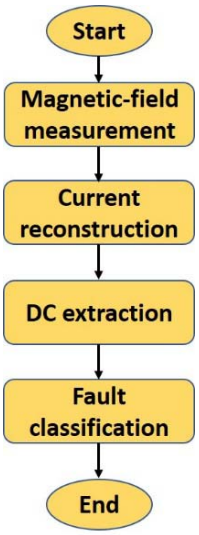


Fig. 7. Flowchart of implementing the method.

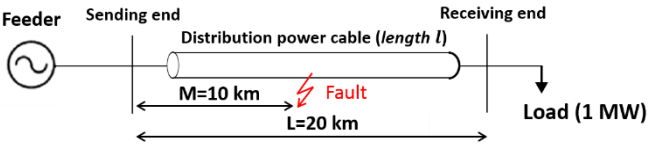


Fig. 8. Power distribution network comprised of a feeder, a 20-km three-phase three-core power distribution cable, and the loading. The fault occurred at 10 km away from the feeder.

Thus, the overall procedure for implementing this technique is shown in Fig. 7. First, the magnetic fields around the surface of a power distribution cable are measured. Then, the magnetic fields are used to reconstruct the current by the stochastic optimization shown in Fig. 5. Afterward, the MM method is deployed to extract the potential dc components in phase currents. Finally, the fault type is classified based on the condition shown in Table III.

## III. Simulation Validation

The proposed fault-classification method was tested on a typical power distribution network in the simulation, as shown in Fig. 8, which consists of a voltage feeder, a 22-kV three-phase three-core distribution power cable, and

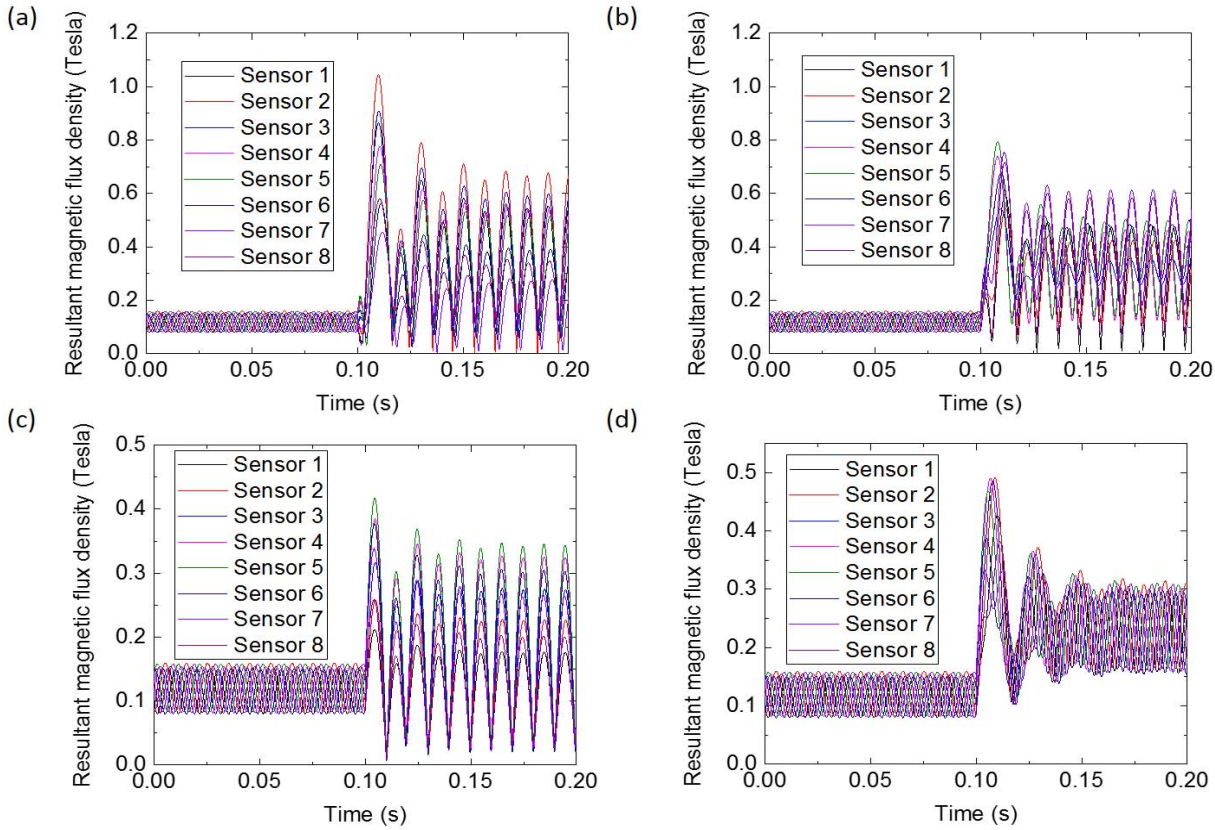


Fig. 9. Resultant magnetic fields measured around the cable surface by the magnetic sensors placed 60 mm from the cable center in various fault types. (a) Phase-to-ground short-circuit fault (A-G). (b) Phase-phase-to-ground short-circuit fault (B-C-G). (c) Phase-to-phase short-circuit fault (B-C). (d) Three-phase short-circuits fault (A-B-C).

TABLE IV
PARAMETER OF POWER DISTRIBUTION NETWORK

| Feeder | | Power Distribution Cable | | |
|---|---|---|---|---|
| Voltage (kV) | 22 | | Positive Sequence | Zero Sequence |
| Short Circuit Capacity (MVA) | 2.2 | Resistance (Ω/km) | 0.024 | 0.412 |
| Inductance (H) | 0.35 | Inductance (mH/km) | 0.4278 | 1.5338 |
| Resistance (Ω) | 13.96 | Capacitance ($\mu F/km$) | 0.2811 | 0.1529 |

the loading (1 MW). The electrical parameters for the feeder and the power distribution cable are listed in Table IV [40]. The total length of the power distribution cable was 20 km, and the fault occurred at 10 km away from the feeder side. The sensing platform was installed at the front end of the cable. Four short-circuit fault types, i.e., phase-to-ground short-circuit fault (A-G), phase-to-phase short-circuit fault (B-C), phase-phase-to-ground short-circuit fault (B-C-G), and three-phase short-circuit fault (A-B-C) were simulated at 0.10 s.

The magnetic fields around the cable surface were measured by a circular array of eight magnetic sensors that were evenly distributed around the cable surface under these four short-circuit fault types (Fig. 9). The three-phase currents were reconstructed from the measured magnetic fields, as shown in Fig. 10. Then, the MM method was applied to extract the dc component after the fault occurred. The fault-classification results are elaborated as follows: 1) a large dc component ($\sim$+63 A) was found at 0.109 s in Phase A after the fault happened at 0.10 s, indicating this was a phase-to-ground short-circuit fault (A-G) [Fig. 10(a)]; 2) dc components were observed for Phases B ($-$46 A at 0.105 s) and C ($\sim-$10 A at 0.102 s) of the same polarity, disclosing this was a phase-phase-to-ground short-circuit fault among Phases B and C and the ground [Fig. 10(b)]; 3) the phase-to-phase short-circuit fault was shown in Fig. 10(c) since the dc components of opposite polarity in Phases B ($\sim-$29 A at 0.104 s) and C ($\sim$+26 A at 0.103 s) were seen; and 4) a three-phase short-circuit fault was shown in Fig. 10(d) by observing dc components in Phase A ($\sim$+69 A at 0.109 s), Phase B ($\sim-$64 A at 0.105 s), and Phase C ($\sim-$20 A at 0.102 s), respectively. The extracted dc component by the MM method matched with the actual values in the faulted phases and the fault types were successfully indicated.

In reality, the measured magnetic signals to be processed for current reconstruction can be contaminated by intrinsic noises/errors of magnetic sensors (e.g., offset error, hysteresis error, and various sources of noise in sensor) or the

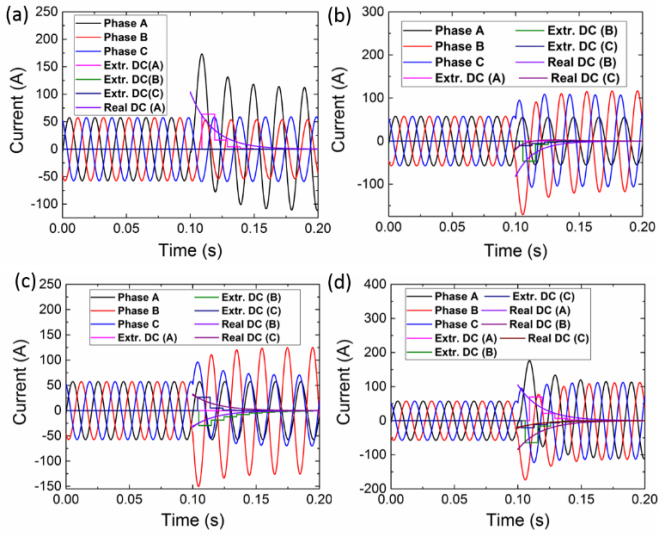


Fig. 10. Reconstructed three-phase currents with the extracted and real dc component in various fault types. (a) Phase-to-ground short-circuit fault (A-G). (b) Phase-phase-to-ground short-circuit fault (B-C-G). (c) Phase-to-phase short-circuit fault (B-C). (d) Three-phase short-circuit fault (A-B-C).

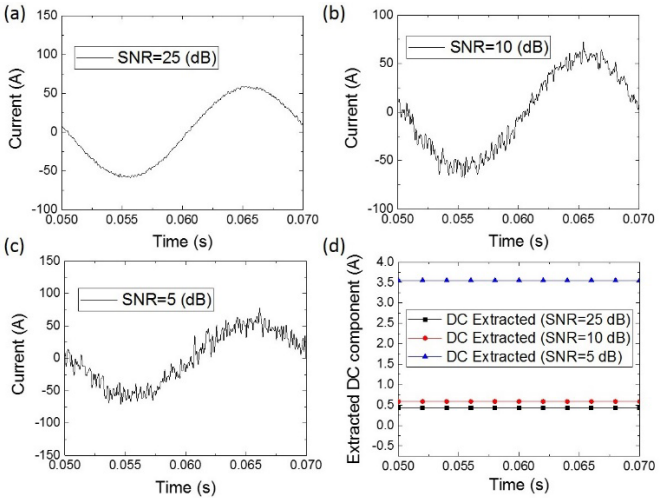


Fig. 11. Influence of noise on current reconstruction. (a) Phase current reconstructed from noisy magnetic-field measurement at SNR = 25. (b) Phase current reconstructed from noisy magnetic-field measurement at SNR = 10. (c) Phase current reconstructed from noisy magnetic-field measurement at SNR = 5. (d) DC component extracted from the reconstructed phase current based on noisy magnetic-field measurement (SNR = 25, 10, and 5 dB).

background electromagnetic noises. To investigate the influence of noises, signal-to-noise ratios at different levels (25–40-dB SNR represent very good signals, 15–25-dB SNR good signals, 10–15-dB SNR low signals, and 5–10-dB SNR bad signals [41]) were added into the magnetic-field measurement in the steady status of the system configuration in Fig. 8. A cycle of phase current reconstructed from magnetic-field measurement under several noise levels (SNR = 25, 10, and 5 dB) is shown in Fig. 11. It can be seen that the reconstructed currents became more fluctuated as the noise level increased [Fig. 11(a)–(c)]. The extracted dc components also became stronger accordingly (0.43, 0.58, and 3.55, respectively), as shown in Fig. 11(d), because the asymmetry

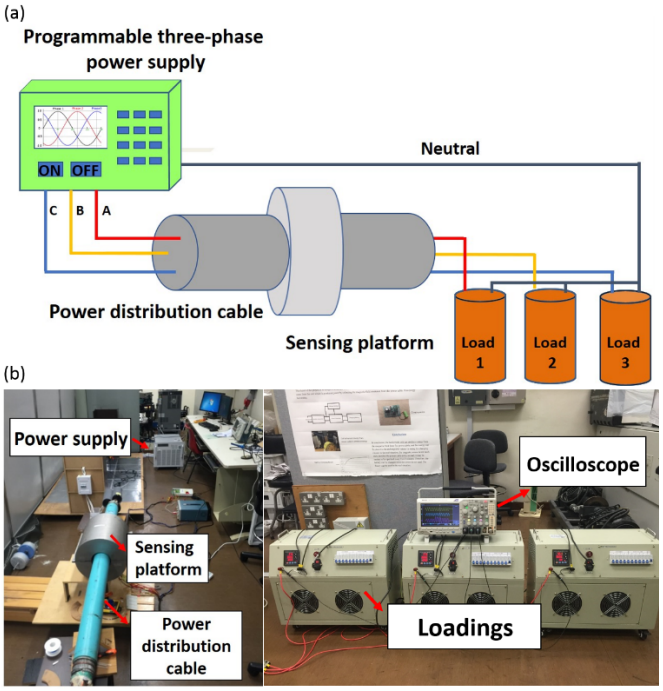


Fig. 12. Experimental setup for validating the proposed fault-classification method. (a) Schematic of the testing platform comprised of a programmable power source, a power distribution cable, loadings, and a sensing platform. (b) Hardware of the testing platform.

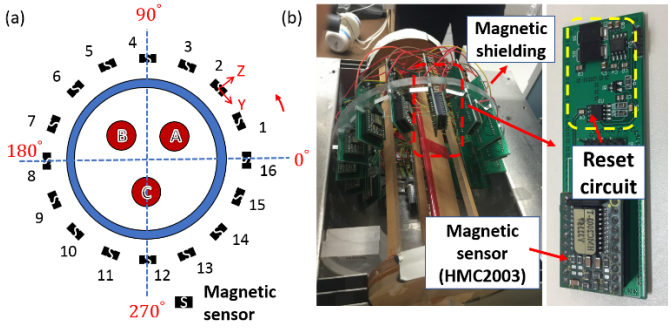


Fig. 13. Magnetic field measurement. (a) Array of 16 magnetic sensors around the cable surface to measure $y$- and $z$-axes magnetic fields. (b) Hardware of sensing platform comprised of magnetic sensors, reset circuit, and magnetic shielding.

of current increased due to the noise. This will introduce a dc component in the steady status of system operation, which can confuse the proposed method. Therefore, it is necessary to eliminate the background magnetic disturbances (e.g., installing a magnetic shielding).

## IV. Experimental Validation and Discussion

The experiment was conducted in the lab to verify the practical feasibility of the proposed method for the fault classification of power distribution cables. The schematic of the experimental setup comprised of a power supply, a power distribution cable, a sensing platform, and the loadings is shown in Fig. 12(a). The power distribution cable was energized by a programmable power source (61704, Chroma) and connected with resistive loadings [Fig. 12(b)]. The voltage

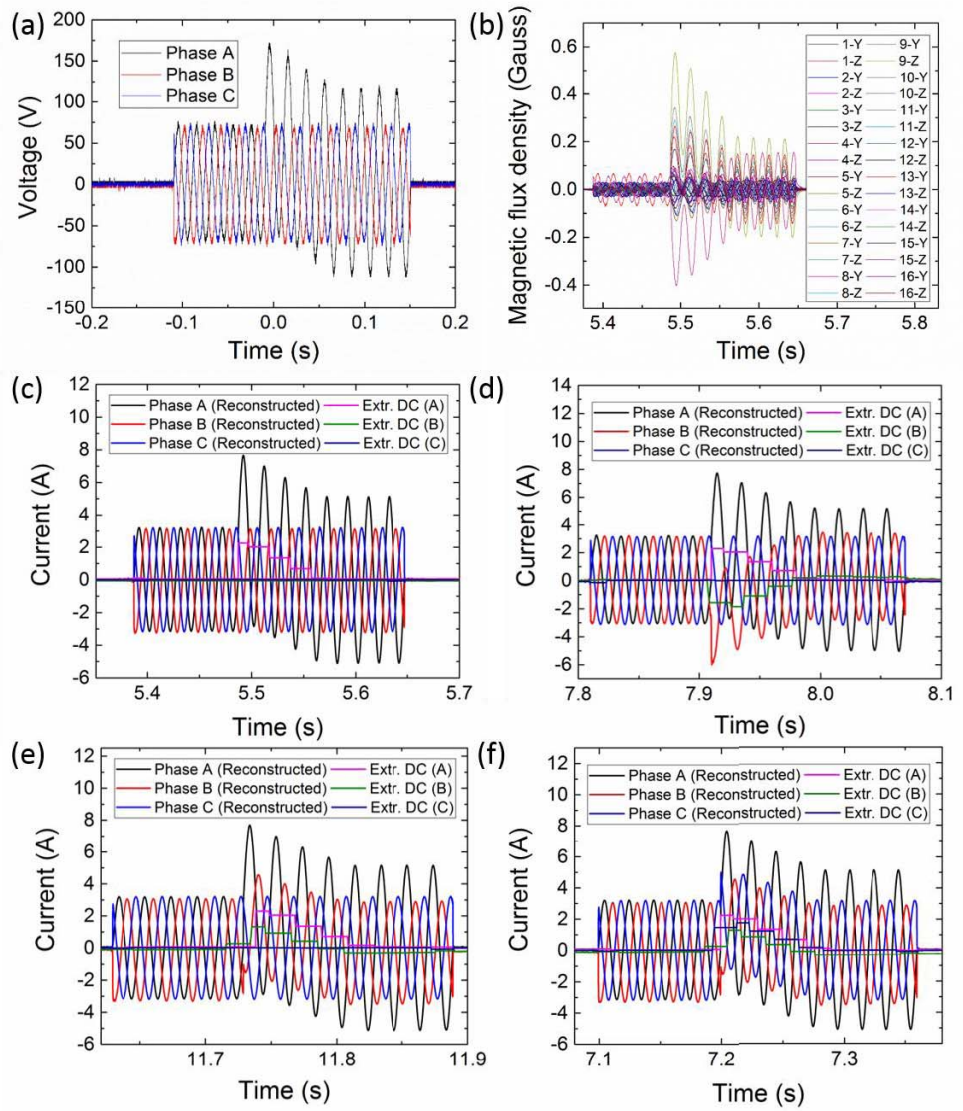


Fig. 14. Reconstructed three-phase currents with the extracted and real dc component in various fault types. (a) Programmed voltage waveform of a phase-to-ground fault (A-G). (b) Responses of magnetic sensors in the $y$- and $z$-axes under the phase-to-ground fault (A-G). (c) Reconstructed dc components for phase-to-ground short-circuit fault (A-G). (d) Reconstructed dc components for phase-to-phase short-circuit fault (A-B). (e) Reconstructed dc components for phase-to-ground short-circuit fault (A-B-G). (f) Reconstructed dc components for three-phase short-circuit fault (A-B-C).

generated by the programmable power source was measured using an oscilloscope (DPO 2024B, Tektronix) connecting with the loadings. The sensing platform comprised of a magnetic sensor array around the cable surface was shown in Fig. 13(a). The off-the-shelf three-axis magnetoresistive sensors (HMC2003 [42], [43]) were deployed for their ideal features such as high resolution (40 $\mu$gauss) and integrated condition circuit. The $x$-axis of the sensor was along the cable axial direction, while the $y$- and $z$-axes of the sensors were located in a plane to measure the orthogonal magnetic field. Regarding the algorithm in Fig. 5, the number of magnetic-sensing points can affect the reconstruction accuracy, since the measured magnetic fields are used to evaluate the magnetic fields emanated from the optimized currents. Therefore, more magnetic sensors can provide more information for reconstruction in principle; however, it also adds the hardware cost. We have demonstrated that the errors are reduced with the number of sensors. Increasing the number of sensors beyond 16 only brought very small further reduction in error [44]. Therefore, 16 magnetic sensors were installed evenly around the cable surface in the experiment and they were numbered anticlockwise. To ensure the same sensing characteristic of these sensors, the circuit of reset function was integrated on the board [Fig. 13(b)]. More details about the set/reset circuit design can be found in [45]. To protect the magnetic signals from the environment, a magnetic shielding was also installed outside the magnetic sensor array, and its effectiveness has been verified [33].

The proposed method was validated in four short-circuit fault types, namely, phase-to-ground short-circuit fault (A-G), phase-to-phase short-circuit fault (A-B), phase-phase-to-ground short-circuit fault (A-B-G), and three-phase short-circuit fault (A-B-C). The specific current waveforms of these faults were generated by programming the power supply.

For example, the voltage waveform of a phase-to-ground fault (A-G) was shown in Fig. 14(a), wherein the voltage of Phase A increased to a large extent after fault while the other phases remained almost unchanged. This results in the same pattern of current waveform in the circuit under the resistive loadings. The responses of magnetic sensors in the $y$- and $z$-axes under this phase-to-ground fault are shown in Fig. 14(b). With the measured magnetic fields, the three-phase currents were reconstructed and the MM method was adopted to extract the dc components for each phase. The result in Fig. 14(c) shows that a large dc component existed in Phase A ($\sim$+2.2 A), while it almost could not be found for Phases B ($\sim$+0.003 A) and C ($\sim$+0.027 A). As such, it was identified as a phase-to-ground fault successfully. Similarly, dc components were found for Phases A ($\sim$+2.3 A) and B ($\sim-1.5$ A) of the opposite polarity after the fault in Fig. 14(d), disclosing this is a phase-to-phase short-circuit fault between Phases A and B. The phase-phase-to-ground fault was shown in Fig. 14(e), since the dc components of identical polarity in Phases A ($\sim$+2.3 A) and B ($\sim$+1.3 A) were observed. A three-phase short-circuit fault was shown in Fig. 14(f) by observing dc components in Phase A ($\sim$+2.2 A), Phase B ($\sim$+1.3 A), and Phase C ($\sim-1.4$ A), respectively. These extracted dc components in faulted phases successfully indicated the fault types, verifying the practical feasibility of the proposed method.

To demonstrate the advantage of the proposed method, the experimental results (Fig. 14) were also analyzed and compared with some existing methods in Table I.

1) Comparing With the Overcurrent Method: The overcurrent threshold is set 1.5 times (according to [15]) as the steady current (3.0 A), namely, 4.5 A. The phase-to-ground fault (A-G) can be recognized, since only Phase A (peak of Phase A is 7.66 A after fault) is larger than the threshold. This method can still recognize the phase-to-ground short-circuit fault (A-B-G) since both Phases A and B are larger than the threshold (peak of Phase A is 7.54 A, Phase B is $-6.01$ A, and Phase C is $-3.08$ A after fault). However, it fails to identify the phase-to-ground short-circuit fault (A-B-G) since Phase B cannot reach the threshold (the peak of Phase B is 4.37 A, which is below 4.5 A). It may also malfunction in the three-phase short-circuit fault (A-B-C) because Phase B is lower than the threshold (the peak of Phase B is 4.45 A, which is smaller than the threshold 4.50 A. This result demonstrated that the overcurrent method is not effective due to the subjective threshold setting.
2) Comparing With the Angular Difference Method and Phase Difference Method: Since the angular differences are symmetrical in both normal operation status and three-phase short-circuit fault ($\omega_{AB}, \omega_{BC}, \omega_{AC} \approx 120^{\circ}$) as the normal status, the three-phase short-circuit fault cannot be identified by the angular difference method or the phase difference method.
3) Comparing With Current-Wavelet-Spectrum Method: The wavelet coefficient differs between the healthy and faulted phases of current because the short-circuit fault causes high-frequency signals [46]. An example is shown in Fig. 15 where the faulted and healthy currents in phase-to-ground fault [Fig. 14(b)] are decomposed. The decomposition level is set as 3 (CA3: 0–3.125 kHz; CD3: 3.125–6.25 kHz; CD2: 6.25–12.5 kHz; CD1: 12.5–25 kHz) with wavelet db3. The results disclose that the wavelet coefficients for faulted current are much larger than the ones in the healthy current in the high-frequency bandwidth (e.g., $\sim$0.1 in CD2 for faulted phase while only $\sim$0.01 for healthy phase, and $\sim$0.1 in CD1 for faulted phase while only $\sim$0.004 for healthy phase). Though the faulted and healthy currents can be distinguished by this method, the thresholds for distinguishing the wavelet coefficients in the high frequency vary from system to system. As such, this method is not universal and it requires precalibration.

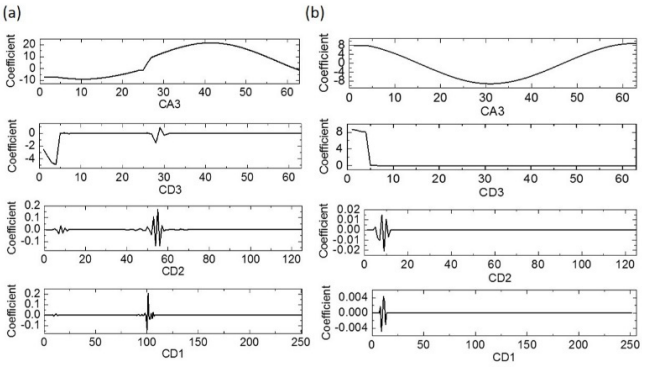


Fig. 15. Wavelet analysis for faulted and healthy currents at a sampling frequency of 25 kHz. (a) Wavelet coefficients for faulted phase (Phase A) in phase-to-ground fault (A-G). (b) Wavelet coefficients for healthy phase (Phase B) in phase-to-ground fault (A-G).

From the above comparison, we can see that the proposed method exhibits promising advantages over the traditional ones. Further comparison with the high-frequency energy method and high-frequency noise in the EMI environment will be conducted within a substation with a real background of electromagnetic field noise in the future.

## V. Conclusion

In this paper, a new fault-classification technique by detecting decaying dc components in fault currents with magnetic sensing was proposed and verified. The dc component was extracted by the MM method from the current reconstructed by magnetic sensing. The feasibility of the method was validated both by simulation and experiment. This method does not require precalibration in terms of network, does not suffer the dc bias issue as in CTs [47], is invulnerable to EMI, and can reliably identify three-phase short-circuit faults. The impacts of this method are summarized as follows. First, the reliability of fault classification in distribution networks can be enhanced for ensuring the proper function of relays and facilitating the repair work. Second, the workforce of the precalibration process for installing relays on each underground power cable can be eliminated, and thus the power system can be more cost-effective. Last but not the least, this work can facilitate the smart grid construction by improving the self-healing ability

in distribution systems and boost the smart city development by safeguarding the continuity of power supply [48], [49].

The technique will be tested under different conditions (e.g., different fault times, fault distances, and locations, and network voltage) in a real on-site environment of a power system to validate its practical effectiveness in the future work.

## REFERENCES


[1] L. S. Czarnecki and Z. Staroszczyk, "On-line measurement of equivalent parameters for harmonic frequencies of a power distribution system and load," *IEEE Trans. Instrum. Meas.*, vol. 45, no. 2, pp. 467–472, Apr. 1996.

[2] T. Gönen, *Electric Power Distribution System Engineering*. New York, NY, USA: McGraw-Hill, 1986.

[3] K. Zhu, W. K. Lee, and P. W. T. Pong, "Non-contact voltage monitoring of HVDC transmission lines based on electromagnetic fields," *IEEE Sensors J.*, vol. 19, no. 8, pp. 3121–3129, Apr. 2019.

[4] S. C. Chu, "Screening factor of pipe-type cable systems," *IEEE Trans. Power App. Syst.*, vol. PAS-88, no. 5, pp. 522–528, May 1969.

[5] O. Quiroga, J. Meléndez, and S. Herraiz, "Fault causes analysis in feeders of power distribution networks," in *Proc. Int. Conf. Renewables Energies Qual. Power*, 2011, p. 9.

[6] K. Zhu, W. K. Lee, and P. W. T. Pong, "Fault-line identification of HVDC transmission lines by frequency-spectrum correlation based on capacitive coupling and magnetic field sensing," *IEEE Trans. Magn.*, vol. 54, no. 11, pp. 1–5, Nov. 2018.

[7] P. K. Dash, S. R. Samantaray, and G. Panda, "Fault classification and section identification of an advanced series-compensated transmission line using support vector machine," *IEEE Trans. Power Del.*, vol. 22, no. 1, pp. 67–73, Jan. 2007.

[8] A. de Souza Gomes, M. A. Costa, T. G. A. de Faria, and W. M. Caminhas, "Detection and classification of faults in power transmission lines using functional analysis and computational intelligence," *IEEE Trans. Power Del.*, vol. 28, no. 3, pp. 1402–1413, Jul. 2013.

[9] V. S. Kale, S. R. Bhide, and P. P. Bedekar, "Faulted phase selection on double circuit transmission line using wavelet transform and neural network," in *Proc. Int. Conf. Power Syst.*, Dec. 2009, pp. 1–6.

[10] H. Shu, Q. Wu, X. Wang, and X. Tian, "Fault phase selection and distance location based on ANN and S-transform for transmission line in triangle network," in *Proc. 3rd Int. Conf. Image Signal Process.*, Oct. 2010, pp. 3217–3219.

[11] Z. Q. Bo, R. K. Aggarwal, A. T. Johns, H. Y. Li, and Y. H. Song, "A new approach to phase selection using fault generated high frequency noise and neural networks," *IEEE Trans. Power Del.*, vol. 12, no. 1, pp. 106–115, Jan. 1997.

[12] W. M. Al-hassawi, N. H. Abbasi, and M. M. Mansour, "A neural-network-based approach for fault classification and faulted phase selection," in *Proc. Can. Conf. Elect. Comput. Eng.*, May 1996, pp. 384–387.

[13] P. Gill, *Electrical Power Equipment Maintenance and Testing*. Boca Raton, FL, USA: CRC Press, 2008.

[14] F. B. Costa, B. A. Souza, and N. S. D. Brito, "A wavelet-based method for detection and classification of single and crosscountry faults in transmission lines," in *Proc. Int. Conf. Power Syst. Transients*, Jun. 2009, pp. 1–8.

[15] NPTEL. (2019). *Overcurrent Protection*. Accessed: Mar. 13, 2019. [Online]. Available: https://nptel.ac.in/courses/108101039/download/Lecture-15.pdf

[16] J. Faiz, S. Lotfi-fard, and S. H. Shahri, "Prony-based optimal Bayes fault classification of overcurrent protection," *IEEE Trans. Power Del.*, vol. 22, no. 3, pp. 1326–1334, Jul. 2007.

[17] A. Ferrero and G. Superti-Furga, "A new approach to the definition of power components in three-phase systems under nonsinusoidal conditions," *IEEE Trans. Instrum. Meas.*, vol. 40, no. 3, pp. 568–577, Jun. 1991.

[18] D. Middleton, "Statistical-physical models of electromagnetic interference," *IEEE Trans. Electromagn. Compat.*, vol. EMC-19, no. 3, pp. 106–127, Aug. 1977.

[19] T. Adu, "An accurate fault classification technique for power system monitoring devices," *IEEE Trans. Power Del.*, vol. 17, no. 3, pp. 684–690, Jul. 2002.

[20] C. Zheng *et al.*, "Magnetoresistive sensor development roadmap (non-recording applications)," *IEEE Trans. Magn.*, vol. 55, no. 4, pp. 1–30, Apr. 2019.

[21] Y. S. Cho, C. K. Lee, G. Jang, and H. J. Lee, "An innovative decaying DC component estimation algorithm for digital relaying," *IEEE Trans. Power Del.*, vol. 24, no. 1, pp. 73–78, Jan. 2009.

[22] J. Machowski, J. Bialek, and J. Bumby, *Power System Dynamics: Stability and Control*. Hoboken, NJ, USA: Wiley, 2011.

[23] J. Arrillaga and N. R. Watson, *Power System Harmonics*. Hoboken, NJ, USA:Wiley, 2004.

[24] M. Eremia and M. Shahidehpour, *Handbook of Electrical Power System Dynamics: Modeling, Stability, and Control*, vol. 92. Hoboken, NJ, USA: Wiley, 2013.

[25] K. M. Silva, B. A. Souza, and N. S. D. Brito, "Fault detection and classification in transmission lines based on wavelet transform and ANN," *IEEE Trans. Power Del.*, vol. 21, no. 4, pp. 2058–2063, Oct. 2006.

[26] A. Bernieri, G. Betta, and C. Liguori, "On-line fault detection and diagnosis obtained by implementing neural algorithms on a digital signal processor," *IEEE Trans. Instrum. Meas.*, vol. 45, no. 5, pp. 894–899, Oct. 1996.

[27] R. Isermann, *Fault-Diagnosis Systems: An Introduction From Fault Detection to Fault Tolerance*. New York, NY, USA: Springer, 2006.

[28] M. N. Alam, R. H. Bhuiyan, R. A. Dougal, and M. Ali, "Design and application of surface wave sensors for nonintrusive power line fault detection," *IEEE Sensors J.*, vol. 13, no. 1, pp. 339–347, Jan. 2013.

[29] M. J. Devaney and L. Eren, "Detecting motor bearing faults," *IEEE Instrum. Meas. Mag.*, vol. 7, no. 4, pp. 30–50, Dec. 2004.

[30] M. Silva, M. Oleskovicz, and D. V. Coury, "A fault locator for transmission lines using traveling waves and wavelet transform theory," in *Proc. 8th IEE Int. Conf. Develop. Power Syst. Protection*, Apr. 2004, pp. 212–215.

[31] P. Dutta, A. Esmaeilian, and M. Kezunovic, "Transmission-line fault analysis using synchronized sampling," *IEEE Trans. Power Del.*, vol. 29, no. 2, pp. 942–950, Apr. 2014.

[32] K. Zhu, W. K. Lee, and P. W. T. Pong, "Non-contact capacitive-coupling-based and magnetic-field-sensing-assisted technique for monitoring voltage of overhead power transmission lines," *IEEE Sensors J.*, vol. 17, no. 4, pp. 1069–1083, Feb. 2017.

[33] K. Zhu, W. Han, W. K. Lee, and P. W. T. Pong, "On-site non-invasive current monitoring of multi-core underground power cables with a magnetic-field sensing platform at a substation," *IEEE Sensors J.*, vol. 17, no. 6, pp. 1837–1848, Mar. 2017.

[34] A. Canova, F. Freschi, M. Repetto, and M. Tartaglia, "Description of power lines by equivalent source system," *Int. J. Comput. Math. Elect. Electron. Eng.*, vol. 24, no. 3, pp. 893–905, 2005.

[35] L. Davis, *Handbook of Genetic Algorithms*. Amsterdam, The Netherlands: Elsevier, 1991.

[36] K. Iba, "Reactive power optimization by genetic algorithm," *IEEE Trans. Power Syst.*, vol. 9, no. 2, pp. 685–692, May 1994.

[37] J. Buse, D. Y. Shi, T. Y. Ji, and Q. H. Wu, "Decaying DC offset removal operator using mathematical morphology for phasor measurement," in *Proc. IEEE PES Innov. Smart Grid Technol. Conf. Eur.*, Oct. 2010, pp. 1–6.

[38] J. Serra, "Introduction to mathematical morphology," *Comput. Vis., Graph., Image Process.*, vol. 35, pp. 283–305, Sep. 1986.

[39] P. Duhamel and M. Vetterli, "Fast Fourier transforms: A tutorial review and a state of the art," *Signal Process.*, vol. 19, no. 4, pp. 259–299, 1990.

[40] A. A. bin M. Zin, J. Tavalaei, and M. H. bin Habibuddin, "Simulation of distance relay operation on fault condition in MATLAB software/simulink," *Proc. Elect. Eng. Comput. Sci. Inform.*, vol. 1, no. 1, pp. 355–360, 2014.

[41] J. Park, A. John Park, and S. Mackay, *Practical Data Acquisition for Instrumentation and Control Systems*. Boston, MA, USA: Newnes, 2003.

[42] K. J. O'Donovan, R. Kamnik, D. T. O'Keeffe, and G. M. Lyons, "An inertial and magnetic sensor based technique for joint angle measurement," *J. Biomech.*, vol. 40, no. 12, pp. 2604–2611, 2007.

[43] Honeywell. (2011). *3-Axis Magnetic Sensor Hybrid HMC2003*. Accessed: 19. Jul, 2018 [Online]. Available: https://neurophysics.ucsd.edu/Manuals/Honeywell/HMC_2003.pdf

[44] K. Zhu, X. Liu, and P. W. T. Pong, "On-site real-time current monitoring of three-phase three-core power distribution cables with magnetic sensing," in *Proc. IEEE Sensors*, Oct. 2018, pp. 1–4.

[45] Honeywell. (2018). *SET/RESET Pulse Circuits for Magnetic Sensors*. Accessed: 19. Jul, 2018. [Online]. Available: https://neurophysics.ucsd.edu/Manuals/Honeywell/AN-201.pdf

[46] A. W. Galli and O. M. Nielsen, "Wavelet analysis for power system transients," *IEEE Comput. Appl. Power*, vol. 12, no. 1, pp. 16–25, Jan. 1999.

[47] M. S. Ballal, M. G. Wath, and H. M. Suryawanshi, "A novel approach for the error correction of CT in the presence of harmonic distortion," *IEEE Trans. Instrum. Meas.*, to be published.
[48] X. Liu *et al.*, "Overview of Spintronic sensors, Internet of things, and smart living," 2016, *arXiv:1611.00317*. [Online]. Available: https://arxiv.org/abs/1611.00317
[49] A. Cocchia, "Smart and digital city: A systematic literature review," in *Smart City*. New York, NY, USA: Springer, 2014, pp. 13–43.

**Ke Zhu** was born in Yichang, China, in 1990. He received the B.Eng. degree in electrical engineering from China Three Gorges University (CTGU), Yichang, in 2013, the Ph.D. degree in electrical and electronic engineering from the University of Hong Kong (HKU), Hong Kong, in 2018.

He is currently a Post-Doctoral Researcher with HKU. His current research interests include computational electromagnetics, electric power transmission monitoring, and application of magnetoresistive (MR) sensors in the smart grid.

Dr. Zhu is a member of the IEEE Magnetics Society (Hong Kong Chapter).

**Philip W. T. Pong** received the B.Eng. degree (First Class Hons.) in electrical and electronic engineering from the University of Hong Kong (HKU), Hong Kong, in 2002, and the Ph.D. degree in engineering from the University of Cambridge, Cambridge, U.K., in 2005.

He was a Post-Doctoral Researcher at the Magnetic Materials Group, National Institute of Standards and Technology (NIST), Gaithersburg, MD, USA. In 2008, he joined the Department of Electrical and Electronic Engineering, HKU, where he is currently an Associate Professor and involved in the development of magnetoresistive (MR) sensors, and the applications of MR sensors in smart grid and smart living.

Dr. Pong serves as a fellow of the Institution of Engineering and Technology, the Institute of Materials, Minerals and Mining, and the NANOSMAT Society, and a corporate member of Hong Kong Institution of Engineers (HKIE) in Electrical Division, Electronics Division and Energy Division. He was a recipient of the HKIE Young Engineer of the Year Award in 2016. He is serving on the Administrative Committee of the IEEE Magnetics Society. He is a Chartered Physicist, a Chartered Energy Engineer, and a Registered Professional Engineer. He serves as an Editorial Board Member for three SCI journals.